CHAPTER III

EXPERIMENTAL TECHNIQUE AND APPARATUS

Introduction

Van der Waals or hydrogen-bonded complexes are formed in a free-jet expansion from the pulsed valve described in Chapter II. The complexes are observed by monitoring the absorption of a tunable, continuous wave (CW) laser beam which is passed through the expansion. Infrared, visible, or ultraviolet lasers could in principle be employed depending on the nature of the atom or molecule which is studied. For the experiments described in this thesis the chromophore is the HF, DF, or HCl vibrational fundamental in a rare-gas hydrogen halide bimolecular cluster, which occurs in the near-infrared between 2.5-3.5 μm.

A schematic diagram of the experimental apparatus is shown in Figure 3.1. Tunable infrared laser light is generated by nonlinear difference frequency mixing of frequency-stabilized Ar^+ and dye lasers. The laser light is split into reference and sample beams for a dual-beam measurement which reduces the effects of laser amplitude noise. The sample beam enters the vacuum chamber and passes two or more times through the free jet

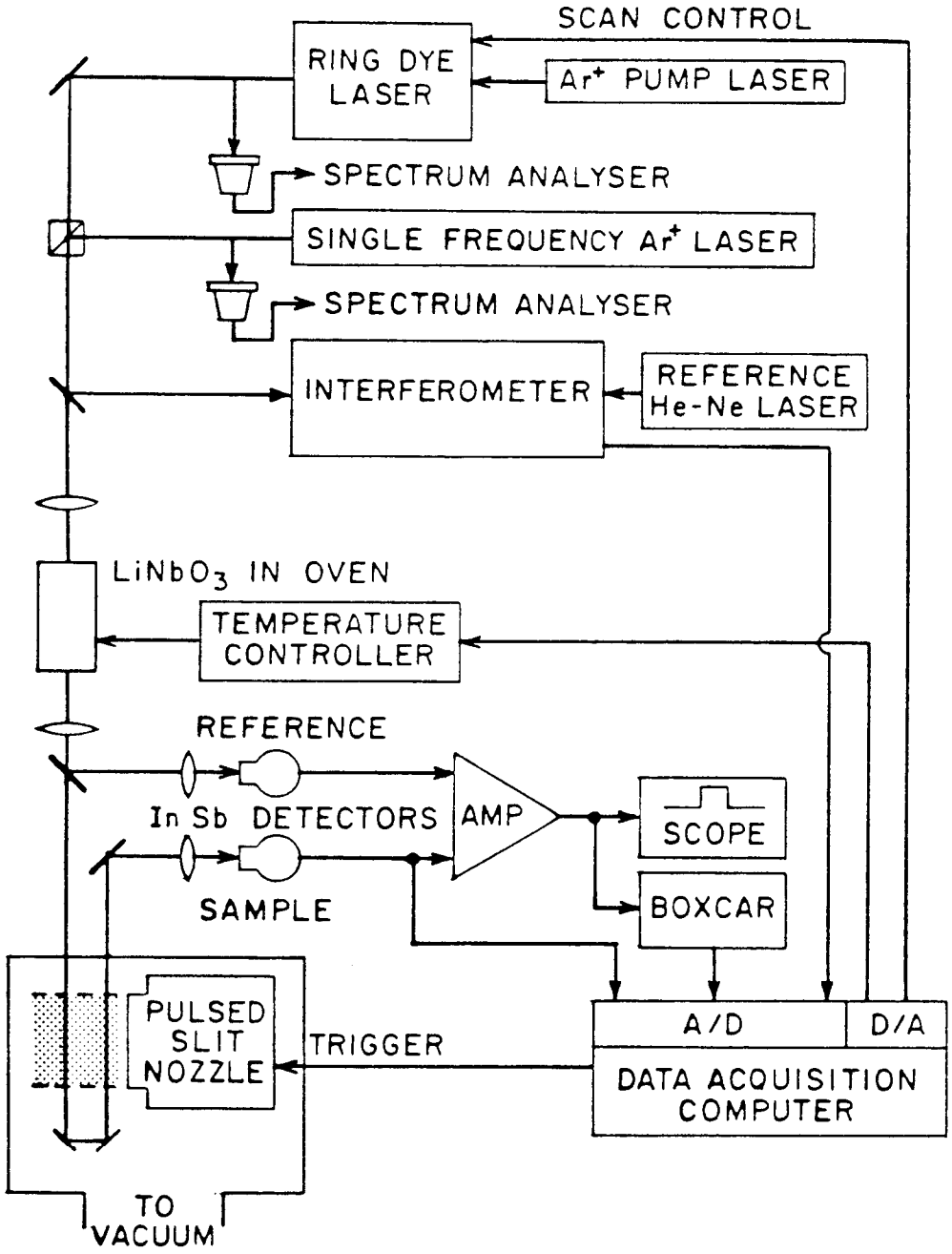

Figure 3.1 Schematic diagram of experimental apparatus.

expansion; sample and reference beams are focused onto matched detectors and the signals subtracted. Transient absorption synchronous with the valve opening is detected as an imbalance of the two beams, which is amplified and averaged with a transient digitizer. Spectra are obtained by recording the absorption as a function of laser frequency. Alternately, individual transition frequencies may be obtained by tuning to the peak of a transition, and measuring simultaneously the Ar^+ and dye laser frequencies with a traveling Michelson interferometer (λ-meter) referenced to known molecular transition frequencies. The experiment is controlled by a computer, which also records and stores the data.

The remainder of this chapter is divided into three sections. First, the infrared laser spectrometer is described. Second, details of the gas handling system are presented. Finally, the important area of frequency measurement is covered in some detail.

Infrared Laser Spectrometer

Infrared Laser Source

A difference frequency laser, similar to that developed by Pine[1] generates CW infrared light tunable from 2.2-4.2 μm. The laser is shown schematically in Figure 3.2. The outputs of a single frequency ring dye laser and a single frequency Ar^+

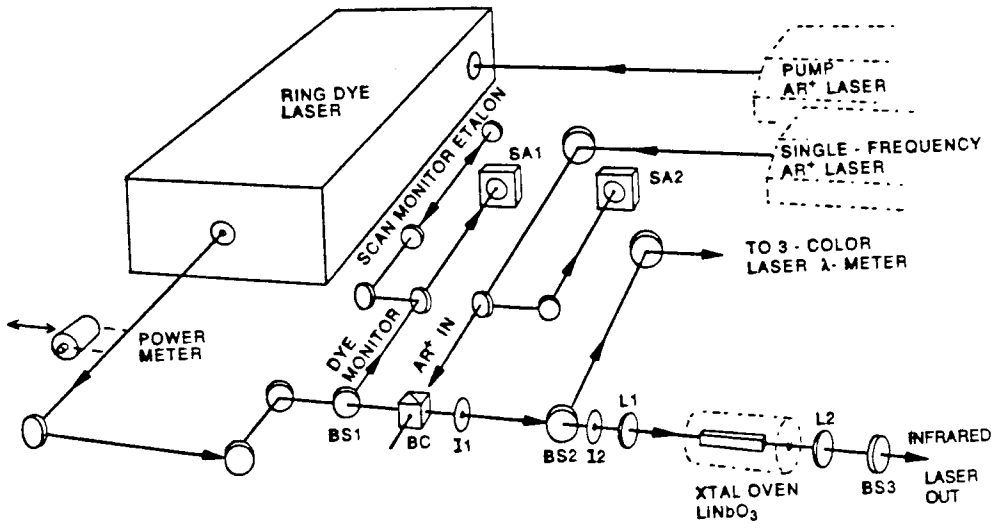

Figure 3.2 Difference frequency laser source.

laser are combined with polarization beam combiner BC, and made collinear by ensuring that both beams are transmitted through irises I1 and I2. The two beams are focused with a 20 cm focal length achromatic lens L1 into a temperature-controlled oven (Chromatix CMX4-IR) containing a 5 cm long $LiNbO_3$ crystal. The $LiNbO_3$ is cut and aligned for 90° phase-matching of the horizontally polarized dye and vertically polarized Ar^+ lasers. The oven temperature is controlled to ±0.05° to maintain the phase-matching conditions, and a flow of oxygen at ≈0.8 standard cubic feet per hour is added to maintain an oxidizing atmosphere which reduces absorption of the visible lasers by contaminants (mostly ferrous iron) in the $LiNbO_3$.

The dye laser is a Spectra Physics 384, which generates 0.10-0.25 W on Rhodamine 6G when pumped by a 4 W Spectra Physics 2020 Ar^+ laser. The Ar^+ laser is a Spectra Physics 2020, 0.40-0.80 W on either the blue-green (488 nm or 20486.8 cm^{-1}) or green (514.5 nm or 19429.9 cm^{-1}) transitions. The nonlinear mixing produces approximately 20 μW of horizontally polarized coherent infrared (IR) light at the difference between the Ar^+ and dye laser frequencies ω_3 and ω_2

$$\omega_1 = \omega_3 - \omega_2 \qquad (3.1)$$

as described by Boyd and coworkers[2,3]. The IR is collimated to a 1.4 mm diameter by a 10 cm focal length CaF_2 lens L2 and

separated from the visible beams by an anti-reflection-coated Ge window BS3. The IR and visible beams are nearly collinear, permitting the use of permanently mounted irises (I2 and others not shown) for convenient alignment.

The infrared frequency is tuned by scanning the dye laser; the Ar^+ frequency is fixed and stabilized by a temperature-stabilized intracavity etalon. A computer-based data acquisition system scans the infrared frequency by sending a digitally generated voltage ramp to the dye laser scan input and to the oven controller.

The infrared laser has frequency noise characteristic of the uncorrelated sum of the dye laser and Ar^+ laser frequency noise,

$$(\Delta\omega_{IR})^2 = (\Delta\omega_1)^2 + (\Delta\omega_2)^2. \qquad (3.2)$$

The Ar^+ and dye laser frequency noise arises from both mechanical and electrical sources (e.g. vibrations due to cooling water flow, variations in power supply current, etc.). As obtained from the manufacturer, the dye laser frequency varies ≈50 MHz peak-to-peak (P-P) and the Ar^+ laser ≈ 2 MHz P-P, on msec or faster timescales.

Figure 3.3 shows the technique used to measure the frequency stability of both the dye and Ar^+ lasers, and also

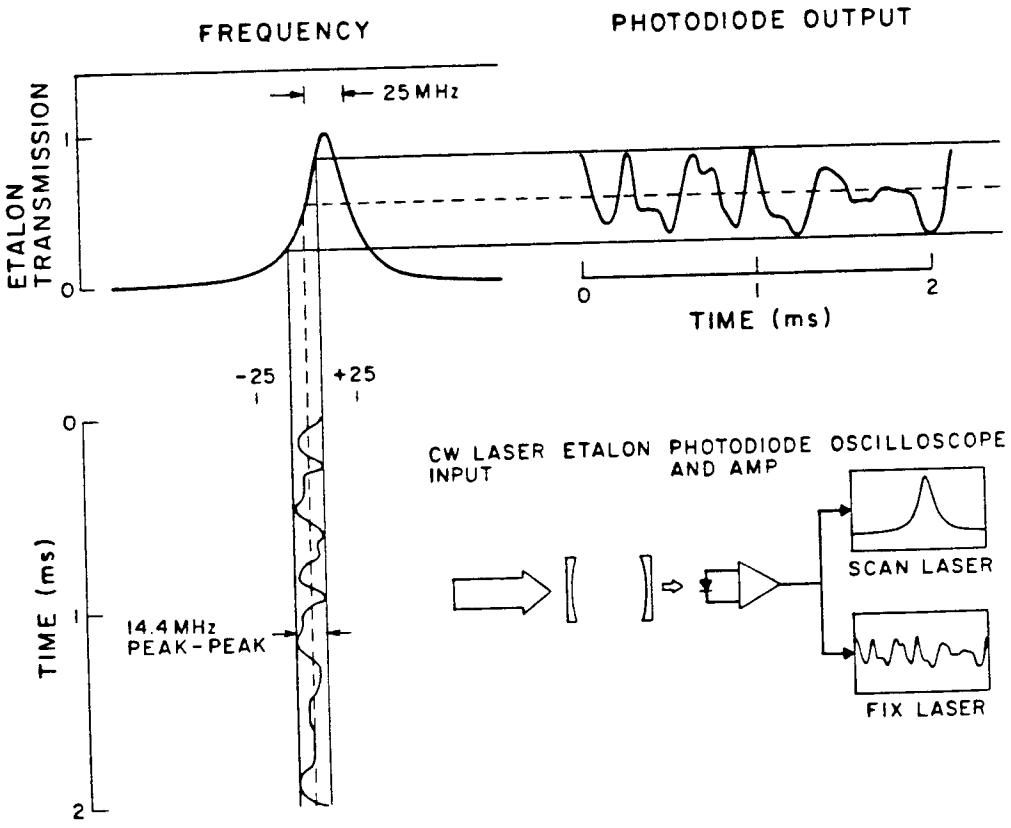

Figure 3.3 Frequency noise measurement using etalon transmission fringe.

demonstrates how the dye laser frequency is controlled. A high finesse ($\gtrsim$ 100) etalon (Spectra Physics Model 450 Laser Spectrum Analyzer) is used as a frequency-to-amplitude converter. The laser frequency is tuned to the side of a transmission fringe, so that frequency excursions about the nominal frequency either increase or decrease the transmitted power. As shown in the figure, the transmitted power P(t) is readily converted to frequency $\omega(t)$ by reference to the profile of a transmission fringe. In the particular example from which the figure was drawn, the transmitted power fluctuates $\approx$ 50% of full scale P-P, equivalent to $\approx$ 14.4 MHz P-P or $\approx$ 3.8 MHz rms.

This diagnostic may be adapted to <u>stabilize</u> the laser frequency, by adding a feedback loop which stabilizes the power transmitted by the etalon. The laser frequency is controlled by mounting one of the cavity mirrors on a piezoelectric transducer (PZT), and varying the voltage applied to the PZT. Increasing voltage lengthens the PZT, shortening the laser cavity. A decrease in the power transmitted by the external etalon is interpreted as a decrease in the laser frequency, and the laser cavity length is decreased to counter this trend. Similarly, an increase in the transmitted power is countered by increasing the laser cavity length. By thus locking the laser frequency to an etalon transmission fringe the infrared frequency excursions are decreased to as low as $\approx$ 2.5 MHz rms, although Figure 3.3

demonstrates a slightly higher value (3.8 MHz). This is approximately 1/16 of the narrowest absorption features observed with the slit nozzle described in Chapter II, and so represents adequate frequency stability for the present experiment. However, other workers have used this etalon fringe locking technique to decrease laser frequency noise to $\lesssim$ 1 Hz!

With the dye laser frequency locked to an etalon transmission fringe, it is necessary to change the etalon spacing to scan the laser frequency. The commercial "spectrum analyzer" to which the laser is locked has a cavity spacing controlled by an internal PZT. This is scanned by applying a computer-generated digital ramp which is separately amplified to 0-1 KVDC.

The scan rate is monitored by recording the transmission fringes of a second etalon. A 46.5 cm long quartz-spaced etalon provides a closely spaced grid (322 MHz, or 0.01074 cm^{-1}) of transmission fringes for frequency interpolation, which are recorded simultaneously with the absorption spectrum. Typical scanning step sizes range from 20 MHz (for rapid survey scans) to 4 MHz (for careful lineshape analysis) which provides 15-75 steps between fringes. Due to nonlinear response of the laser PZT the step size varies by $\approx$15% over a 3 cm^{-1} scan, as determined by counting the number of steps between adjacent etalon fringes. However, the spacing

between adjacent fringes changes very slowly, so the separation between two points on a scan may be interpolated to ≈ 0.001-.0002 cm^{-1}.

Infrared Optical Path

A dual-beam absorption measurement is performed in order to reduce the effect of laser amplitude noise. The IR light from the difference frequency source is split into a sample and reference beam with a CaF_2 substrate, 50% beamsplitter. The sample beam passes two or more times through the jet; both beams are subsequently focused onto matched infrared detectors. The detectors and subsequent electronics are described below.

The beamsplitter which divides the IR light also splits the collinear visible dye laser light, which facilitates the optical alignment described in this section. The entire optical path, from crystal oven to sample chamber to detectors, is enclosed in a plexiglass box which can be purged with dry nitrogen to eliminate or reduce atmospheric water absorption which reduces the transmitted laser power. In general, this is necessary only for the HF complexes, since no significant atmospheric water absorption occurs in the HCl and DF region near ≈3000 cm^{-1}.

A 45 degree, gold coated flat mirror reflects the sample beam into the vacuum chamber containing the slit expansion. Figure 3.4 shows two optical arrangements used to multipass the

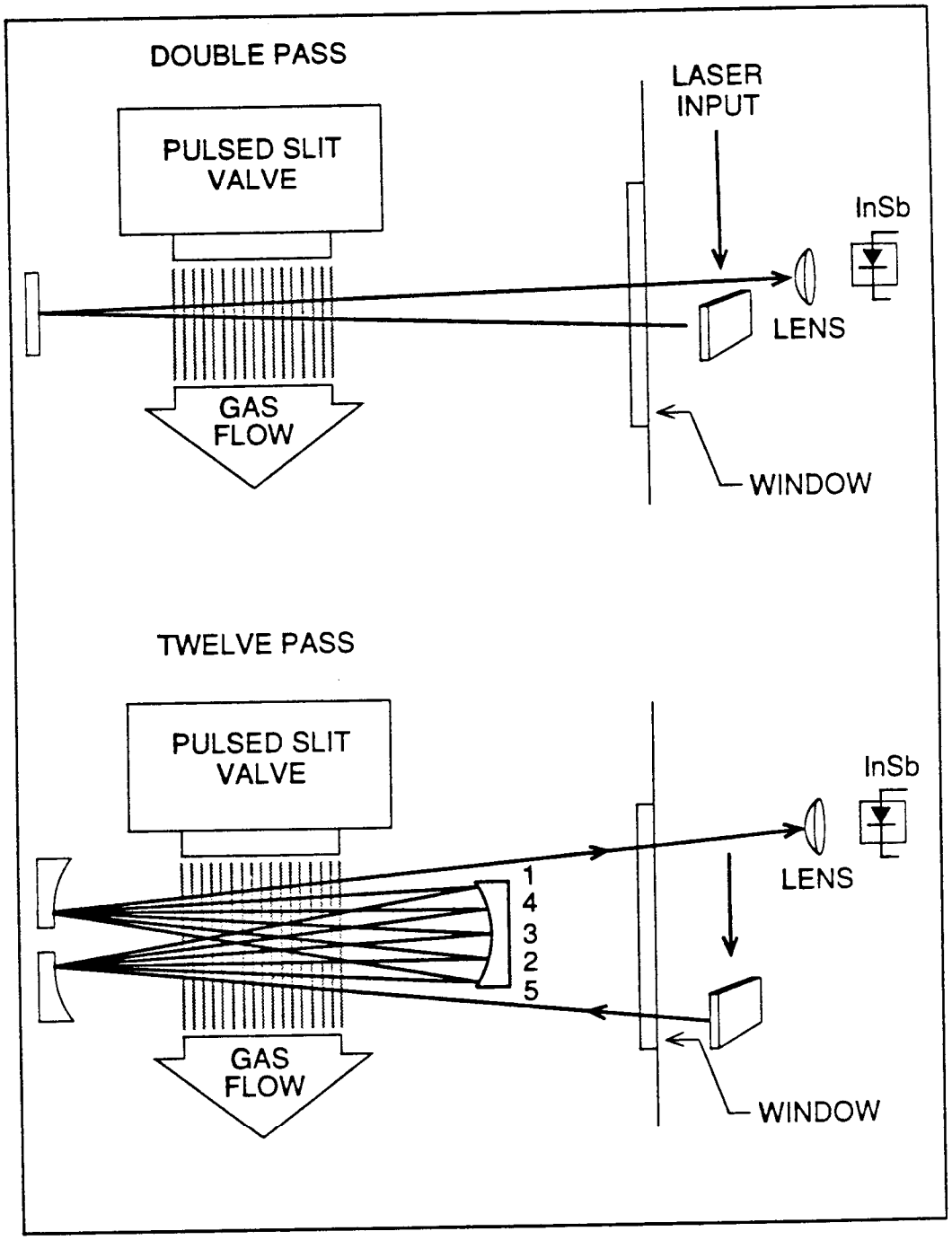

Figure 3.4 Two optical arrangements utilizing slit expansion.

sample beam through the expansion. In the first case, the laser beam passes through the expansion once, is reflected off a flat return mirror, passes through the expansion again nearly parallel to the input beam, exits the vacuum can and is focused onto an infrared detector as described below. The 4 cm long slit nozzle is centered ≈ 8 cm from the return mirror. The small included angle (≈0.5 cm/70cm = 0.0071 rad = 0.41 degrees) between the first and second pass ensures that the two passes nearly overlap; the 1.4 mm diameter beams are separated by only 0.4-0.7 mm. The beams thus sample nearly identical regions of the expansion. This has particular advantages when observing "hot bands" or spectra arising from vibrationally excited states, since both beams can probe very close to the nozzle exit plane where relatively warm conditions are found. Rotational temperatures up to 26° K have been observed in this fashion. However, for general purposes the 8 cm total pathlength does not provide optimal sensitivity.

In the second arrangement the sample beam enters a 12-pass White[4] cell with a 48 cm total absorption pathlength. The White cell consists of three, 30 cm radius gold mirrors separated by 30 cm and arranged as shown in Fig. 3.4. The beam path is also indicated; for the single mirror on the right the multiple reflections are labeled with numbers (1-5) denoting the order in which the reflections occur, while for the two mirrors

on the left the reflections alternately strike the lower and upper mirror. The 12th pass of the laser through the expansion exits the vacuum can.

Although the 12-pass configuration does provide a long pathlength, this is obtained in conjunction with two undesirable side-effects. First, the zig-zag path samples different regions of the expansion, i.e. a region ≈ 0.9 cm along the direction of flow. The gas temperature may differ by as much as a factor of two between the upstream (#12) and downstream (#1) passes if the upstream pass is close to the nozzle exit plane. The intensities might therefore reveal non-equilibrium ro-vibrational distributions. In fact, several examples of non-equilibrium intensity distributions have been observed for the 12-pass geometry (i.e. see Figure 2.23), although not with the two-pass configuration.

Second, as suggested in Fig. 3.4 each pass of the laser through the expansion occurs at a slightly different angle with respect to the jet of gas flowing from the valve. The non-orthogonal crossings produce a Doppler frequency shift $\Delta\omega$ relative to the laboratory frame ω_0

$$\Delta\omega = \omega_0 \frac{v_0}{c} \cos(\theta) \qquad (3.3)$$

where v_0 is the velocity of the jet ($v_0 \approx 5.59\times10^4$ cm/sec for argon diluent), and c is the speed of light. For the two-pass

on the left the reflections alternately strike the lower and upper mirror. The 12th pass of the laser through the expansion exits the vacuum can.

Although the 12-pass configuration does provide a long pathlength, this is obtained in conjunction with two undesirable side-effects. First, the zig-zag path samples different regions of the expansion, i.e. a region ≈ 0.9 cm along the direction of flow. The gas temperature may differ by as much as a factor of two between the upstream (#12) and downstream (#1) passes if the upstream pass is close to the nozzle exit plane. The intensities might therefore reveal non-equilibrium rovibrational distributions. In fact, several examples of non-equilibrium intensity distributions have been observed for the 12-pass geometry (i.e. see Figure 2.23), although not with the two-pass configuration.

Second, as suggested in Fig. 3.4 each pass of the laser through the expansion occurs at a slightly different angle with respect to the jet of gas flowing from the valve. The non-orthogonal crossings produce a Doppler frequency shift $\Delta\omega$ relative to the laboratory frame ω_0

$$\Delta\omega = \omega_0 \frac{v_0}{c} \cos(\theta) \qquad (3.3)$$

where v_0 is the velocity of the jet ($v_0 \approx 5.59\times10^4$ cm/sec for argon diluent), and c is the speed of light. For the two-pass

configuration, $\cos(\theta) \approx 3.5 \times 10^{-3}$, consequently the shift $\Delta\omega \approx$ 0.78 MHz for argon diluent is smaller than the laser linewidth, and can be ignored. However, for the multipass configuration shifts of up to +8.56 MHz for argon diluent are calculated for some of the passes. Table 3.1 summarizes the frequency shifts calculated for each of the 12 optical passes, and the average frequency shift for Ar, Ne, and He diluents. For Ne and particularly for He diluent the absolute shift of the center of the absorption line may be large enough to cause a measurable, systematic frequency shift relative to the laboratory frame of reference. However, since our practice is to measure frequencies relative to references in the free jet expansion, both unknown and reference are shifted by the same amount so no error is introduced. For all three diluents considered below, the different frequency shifts for each pass are also expected to contribute an asymmetry to the lineshape which, however, has not yet been observed experimentally.

Signal Acquisition

A 50% beamsplitter divides the IR output into a reference beam and a sample beam; only the latter passes through the expansion. Subsequently, the two beams are focused with 2.5 cm focal length CaF_2 lenses onto matched 0.04 mm^2 InSb photovoltaic detectors. IR-induced photocurrents ($\approx$ 1

Table 3.1 Frequency shifts for 12-pass White cell configuration.

Optical Pass	Frequency shift (MHz)		
	Ar diluent	Ne diluent	He diluent
1,12	+5.96	+ 8.43	+18.85
2,11	+8.57	+12.11	+27.08
3,10	-4.10	- 5.80	-12.96
4, 9	-5.40	- 7.64	-17.08
5, 8	+0.93	+ 1.32	+ 2.95
6, 7	+2.24	+ 3.16	+ 7.07
Average	+1.37	+ 1.93	+ 4.32

ampere/watt at $\lambda \approx 2.5\ \mu m$) are amplified in matched, home-built amplifiers shown in Figure 3.5, which provide an effective 10^5 volts/watt responsivity (100 KΩ transimpedence). The sample signal is subtracted from the reference in a high common-mode rejection amplifier; the reference channel gain is manually adjusted to minimize the difference between the two inputs. Transient absorption due to complexes formed in the pulsed expansion causes an imbalance of signal and reference beams, which is amplified, signal averaged, and integrated. The data are transferred to a computer for subsequent processing and recording.

The population of an absorbing species is proportional to the absorbance A, defined as

$$A = -\ln\left(\frac{I}{I_0}\right) \tag{3.4}$$

where I_0 is the incident light intensity and $I = I_0 - \Delta I$ is the transmitted light. Equivalently,

$$A = -\ln\left(\frac{I_0 - \Delta I}{I_0}\right) \tag{3.5a}$$

$$= -\ln\left(1 - \frac{\Delta I}{I_0}\right) \tag{3.5b}$$

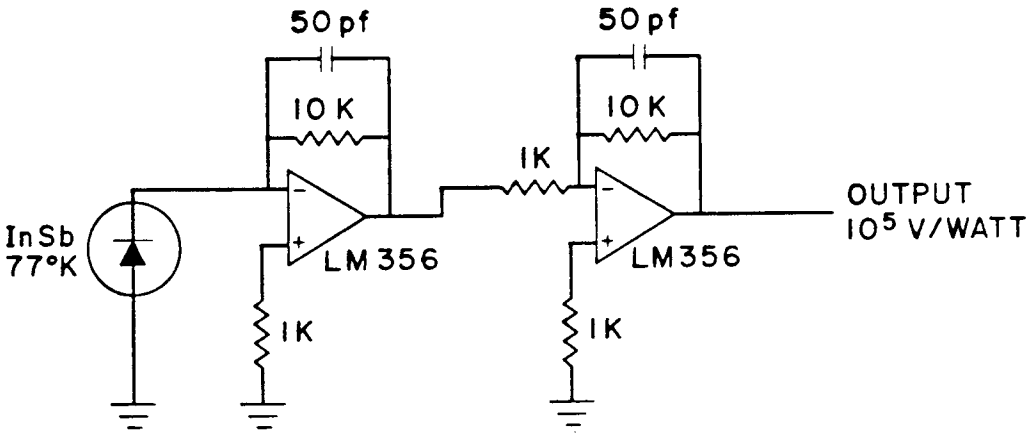

Figure 3.5 Infrared detector and preamplifier circuit.

For small absorbances, Eq.(3.5b) may be approximated as

$$A \approx \frac{\Delta I}{I_0} \tag{3.6}$$

Thus for small absorptions the subtracted signal is directly proportional to the difference ΔI between the output of signal and reference detectors, where the proportionality factor depends on the gain of various amplifiers described below. The transient signal ΔI is therefore normalized to the incident power I_0, which is recorded automatically every 10 frequency steps. For large absorbance the approximation in Eq. (3.6) must be replaced by an approximation of higher order such as

$$A = \frac{\Delta I}{I_0} - \frac{1}{2}\left(\frac{\Delta I}{I_0}\right)^2 + \frac{1}{3}\left(\frac{\Delta I}{I_0}\right)^3 - \ldots \tag{3.7}$$

or by the correct formula Eq. (3.4) using logarithmic amplifiers. Typical absorptions of $\approx 10\%$ in a 48 cm path are observed for strongly allowed transitions of the complexes considered in this work. Use of the approximate formula Eq.(3.6) yields 0.100 versus 0.1054 from Eq. (3.5), a 5% underestimate. This is similar to the measurement reproducibility, and the error decreases for smaller absorbances, so in general corrections are ignored.

Two different high common mode rejection (CMR) amplifiers were used for the subtraction of signal and reference photocurrents. Excellent performance was obtained using a Model

7A18 Tektronix oscilloscope amplifier installed in a Model 7704A oscilloscope. Subsequently, a dedicated home-built differential amplifier was constructed by a dedicated graduate student (see acknowledgements). This amplifier provides performance comparable to (or slightly superior to) the Tektronix oscilloscope, although it requires two adjustments rather than one to balance the gain and maximize the CMR.

An amplitude noise spectrum of the system using the Tektronix oscilloscope is shown in Figure 3.6. The figure shows the root-mean-square (RMS) noise in a 1 Hz bandwidth as a function of the reference frequency, which was obtained by scanning the reference frequency of a lock-in amplifier (Stanford Research Systems Model 510) in RMS voltage mode. The observed noise level, and hence absorption sensitivity, is of the order $10^{-6}/\sqrt{Hz}$ at a detection frequency of 5 kHz. Note that this is within a factor of three of the shot noise limit for 10 μW of infrared light at 2.6 μm, and thus approaches quantum noise limited absorption sensitivity.

The pulsed valve produces an absorption transient which is $\approx$500 μs in duration, at a 20 Hz repetition frequency. The time-dependent absorption signal is filtered with a 3kHz longpass (RC filter) and displayed on an oscilloscope; simultaneously 2-16 pulses per frequency increment are averaged with a transient digitizer (DSP Technology Model 2001S with

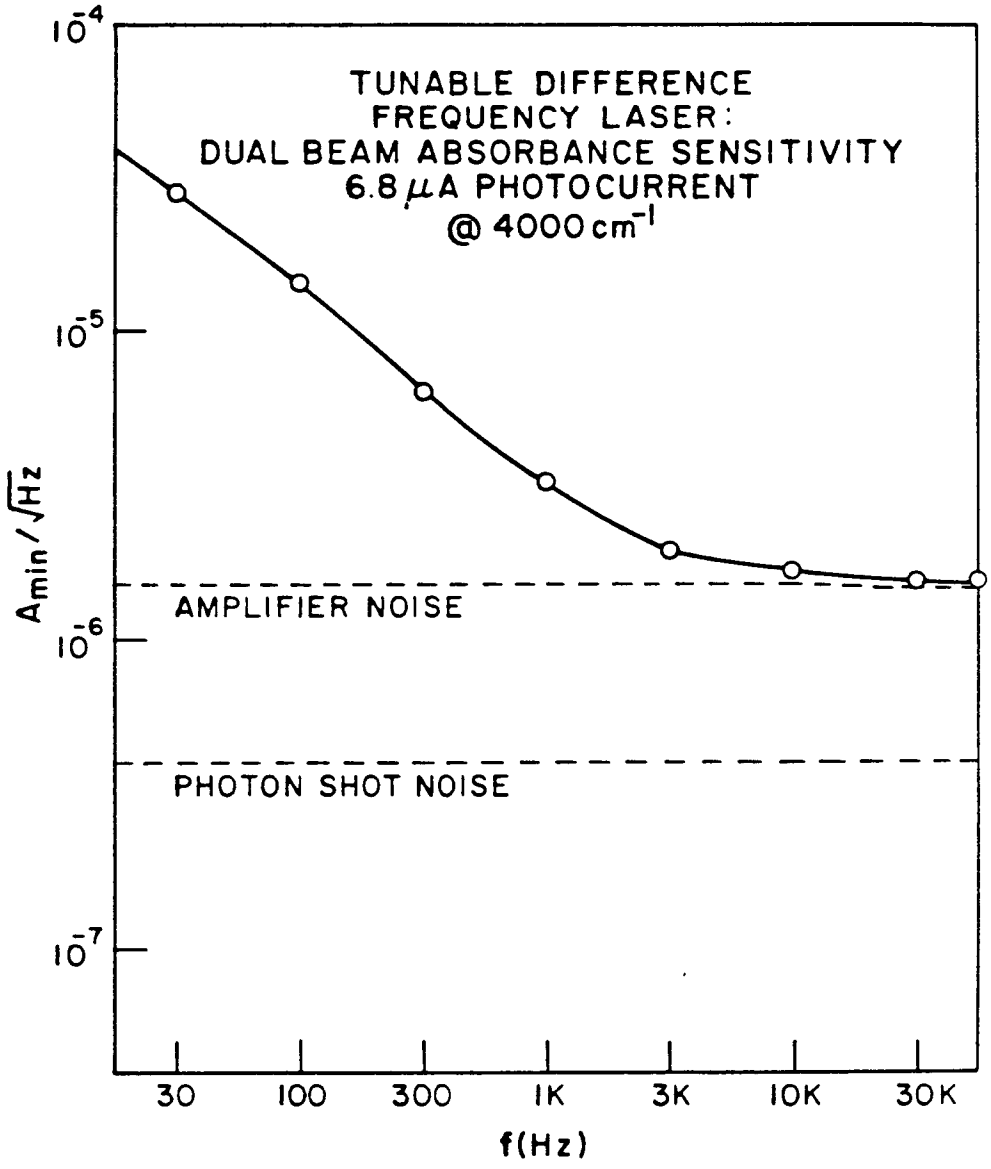

Figure 3.6 Frequency noise characteristics for difference frequency laser source.

Model 4100 Averaging Memory) and portions of the averaged signal are transferred to the computer. Figure 3.7 shows schematically how the transient digitizer signal is divided into three "gates", mimicking a 3-channel boxcar integrator. A 2048 μs signal is recorded at 1 μs/point, roughly centered around the period when the pulsed valve is open. A 512-point sample is obtained during the period the valve is open, and 256-point baseline determinations are obtained before and after the pulse. Baseline fluctuations are reduced by subtracting the two baseline signals from the sample signal. The integration is performed in software, limiting the sampling rate to $\approx$ 60 Hz or $\approx$ 3 times faster than the pulsed valve power supply limit (Figure 2.14).

Imperfect subtraction of fluctuations in infrared power leads to amplitude noise that corresponds to 0.01% absorption using a 500 μs boxcar gate. Single-pulse detection limits of 5 X 10^7 molecules/cm^3/quantum state are estimated for HF and HF-containing complexes using a 48 cm pathlength (12 passes X 4 cm slit length); rotational partition functions Q_r

$$Q_r = \sum_J (2J + 1) \exp \frac{-E(J)}{kT} \qquad (3.8)$$

of 15-150 are observed at jet temperatures of 4-16 Kelvin so detection of total populations of 10^9-10^{10} molecules is typical.

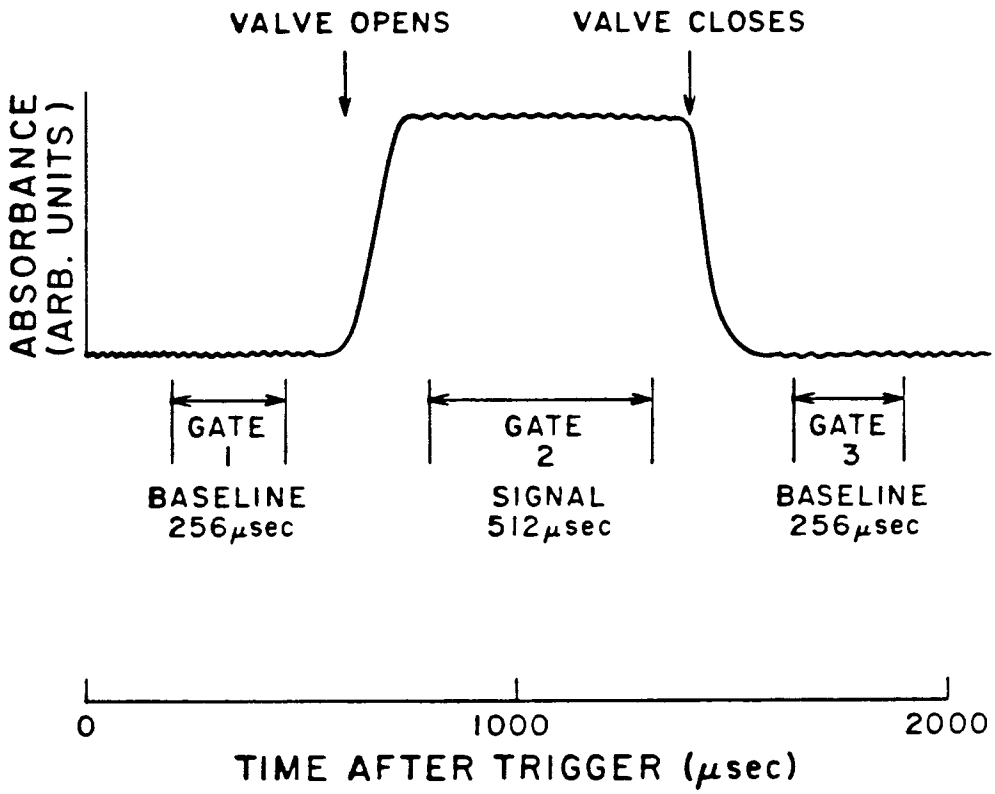

Figure 3.7 Gate settings for time-gated absorption.

Gas handling system

Flow control and gas mixtures

The slit valve uses considerable quantities of gas; 20 Hz operation of a 4 cm × 0.0125 cm slit at typical pressures of 400 Torr argon consumes ≈ 22 standard liters/hour. For helium diluent at a typical 2000 Torr, consumption rises to ≈ 330 standard liters/hour.

Figure 3.8 shows the flow rack built to supply these quantities of gas. Construction is entirely of 300 Series stainless steel since all of the gas mixtures contain the corrosive hydrogen halides HF or HCl. Gas mixtures are metered to a common manifold through a vacuum-compatible pressure regulator (Matheson Model 3602) and regulated to the pulsed valve through a leak valve (Granville-Phillips Model 203). The pressure of gas admitted to the pulsed valve is measured with a capacitance manometer (MKS Baratron Model 222B) with a 0-1000 Torr or 0-10000 range. This combination provides exquisitely sensitive flow control and reproducibility to $\lesssim$ 0.5%. A second leak valve (not shown) and flow meter (Tylan Model FM 380) can be used to add a third component to the gas mixture, however this feature was not used in the experiments described herein.

Mixtures are created in one or two 40-ℓ chambers by

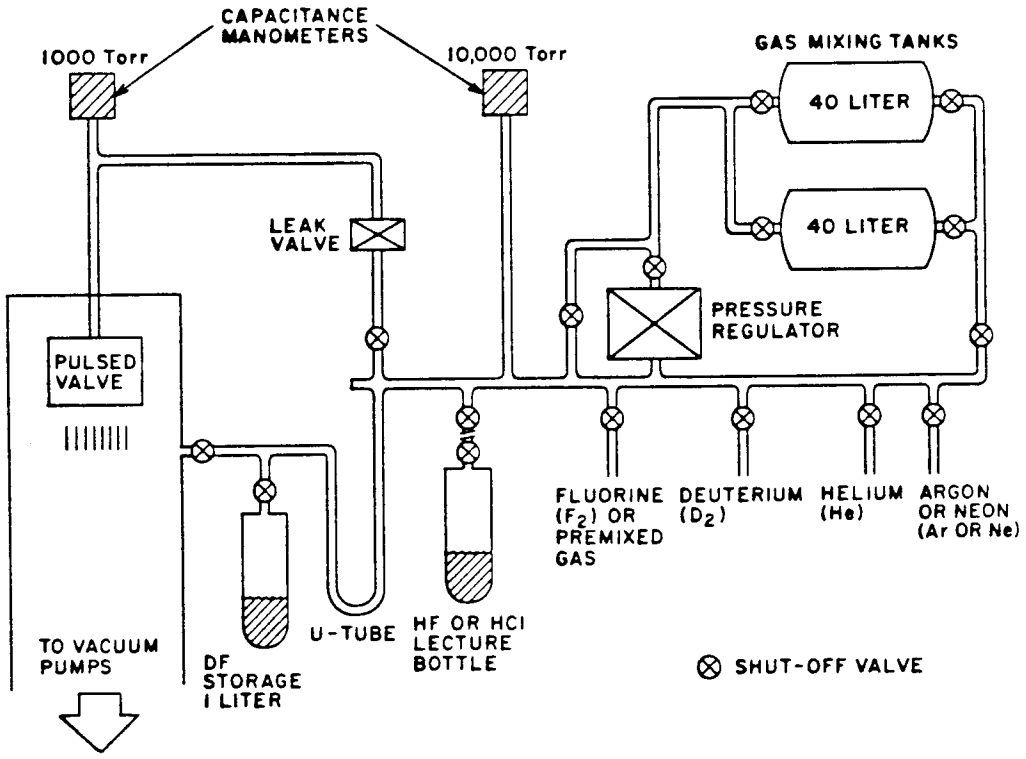

Figure 3.8 Gas handling system for pulsed valve.

adding a measured pressure (typically 25 Torr) of hydrogen halide, then diluting to 2500 Torr with helium (99.995%), neon (70%, balance helium), or argon (99.95%). For safety reasons the cylinder pressure is never allowed to exceed 2500 Torr (≈ 50 pounds per square inch absolute, or PSIA). However, the cylinders were tested at 5000 Torr (≈100 PSIA) by filling with water and then pressurizing with compressed gas; since water is virtually incompressible a cylinder failure during the test would not have decorated the laboratory (or graduate student) with shrapnel.

Mixing is enhanced by rapidly adding rare gas alternately to each end of the cylinder to encourage turbulence. In the absence of turbulent mixing, one must rely on diffusion to disperse the minor species uniformly throughout the mixture. The rate of diffusive mixing is inversely proportional to the pressure; at high pressures this can be a slow process. For example, estimating the diffusion of HCl in Ar from the Ar self-diffusion rate[5] $\bar{D} = 0.0565$ cm^2/sec at 2500 Torr and 300 K, the time constant τ

$$\tau = \frac{x^2}{2D} \qquad (3.9)$$

for mixing over a distance $x \approx 50$ cm is ≈ 6.1 hours! Thus it is better to allow a high-pressure gas mix to homogenize overnight,

even when turbulent mixing is attempted. Since an 80-ℓ supply of such a mixture will last for only $\approx$ 12 hours run time, this is not always practical. A better solution is to use commercial gas mixtures where possible. In the course of these investigations, mixtures of 0.56% HF in He, 0.96% HCl in He, and 0.95% HCl in Ar were obtained from Matheson Gas Products.

For home-brew gas mixtures, HF or HCl ($\gtrsim$ 99%) were purified by repeated freeze-pump-thaw cycles to remove impurities volatile at 77 K (principally H_2 formed by reaction of the hydrogen halide with the walls of the lecture bottle). Commercially available deuterium fluoride (DF) is quite expensive ($\approx$ \$600/mole), especially in the quantities needed (run time at 20 Hz would cost $\approx$ \$6/hour for ArDF, $\approx$ \$110/hour for HeDF!). Consequently, DF is synthesized from the elements

$$D_2 + F_2 \rightarrow 2\ DF \qquad (3.10)$$

in 0.25 mole batches as follows. Approximately 30 Torr of D_2 is first added to the two 40 ℓ mixing tanks. A mixture of 5% F_2 in helium is added over a period of $\approx$ 15 minutes, to a total pressure of 600 Torr. The use of the fluorine-helium mixture minimizes the considerable hazards of handling elemental fluorine, and provides a means of buffering and dissipating the impressive heat release from the reaction ($\approx$ 65 kcal/mole). The reaction proceeds smoothly without need for an external ignition

such as a spark. Additional helium (≈200 Torr) is rapidly added to enhance mixing. Subsequently, the DF is separated from the helium and unreacted gases by trapping in a liquid-nitrogen cooled U-tube (see Figure 3.8), then vacuum-distilled into a 1-ℓ stainless steel storage cylinder.

The small O_2 impurity commonly present in the F_2 forms D_2O, which is also trapped in the U-tube. This is undesirable since water catalyzes the exothermic reaction of DF with the metal of the storage vessel, forming D_2 and metal fluorides. Excess F_2 would displace the oxygen, however the above mixture is slightly D_2 rich to avoid dumping excess F_2 through the vacuum system when the DF is separated. To remove the impurity D_2O the storage vessel contains cobalt trifluoride (Ozark-Mahoning). This powerful oxidizing agent scavenges water from the DF by the reaction

$$3D_2O + 2CoF_3 \rightarrow Co_2O_3 + 6DF \qquad (3.11)$$

Interestingly, trivalent cobalt is the only metal for which the oxide is more stable than the fluoride[6]! The efficacy of this treatment is demonstrated by the lack of measurable D_2 formation ($\lesssim$ 2 Torr) over a 4-week test period. In contrast, the steady decomposition of commercial HF (vapor pressure ≈ 800 Torr) is a well-known safety hazard, as lecture bottles have been known to explode from over-pressure by H_2 formation.

Vacuum Pumps

As mentioned above, flow rates of over 5 standard liters per minute may be encountered with helium diluent. Early trials demonstrated that even with argon diluent it is easy to exceed the flow capacity ($\approx$ 3 Torr-liter/second at 10^{-3} Torr) of a 10" diffusion pump. Fortunately, as described in Chapter 2 the fluid dynamics of the slit expansion permit operation at relatively high pressures ($\lesssim$ 1 Torr) in the vacuum chamber. We use a 1200 cubic feet per minute (CFM) Roots-type "blower", backed with a conventional 125 CFM forepump. Figure 3.9 shows the background pressure in the vacuum chamber for a 4 cm $\times$ 0.0125 cm slit nozzle, operating with 20 Hz, 500 μs pulses (1% duty cycle). Molar flowrates for a supersonic expansion are proportional to the gas pressure and the area of the nozzle (Eq. 2.36); for the highest pressures shown in Figure 3.9 the flowrates are $\approx$0.0046 mole/s He, 0.0015 mole/s Ar at 3000 Torr.

Frequency Measurement

The Ar^+ and dye laser frequencies are measured with a traveling Michelson interferometer constructed after the design of Hall and Lee[7], and shown schematically in Figure 3.10. The Ar^+ and dye laser beams are rendered collinear with the output of a reference HeNe laser using a flat quartz window as a beam

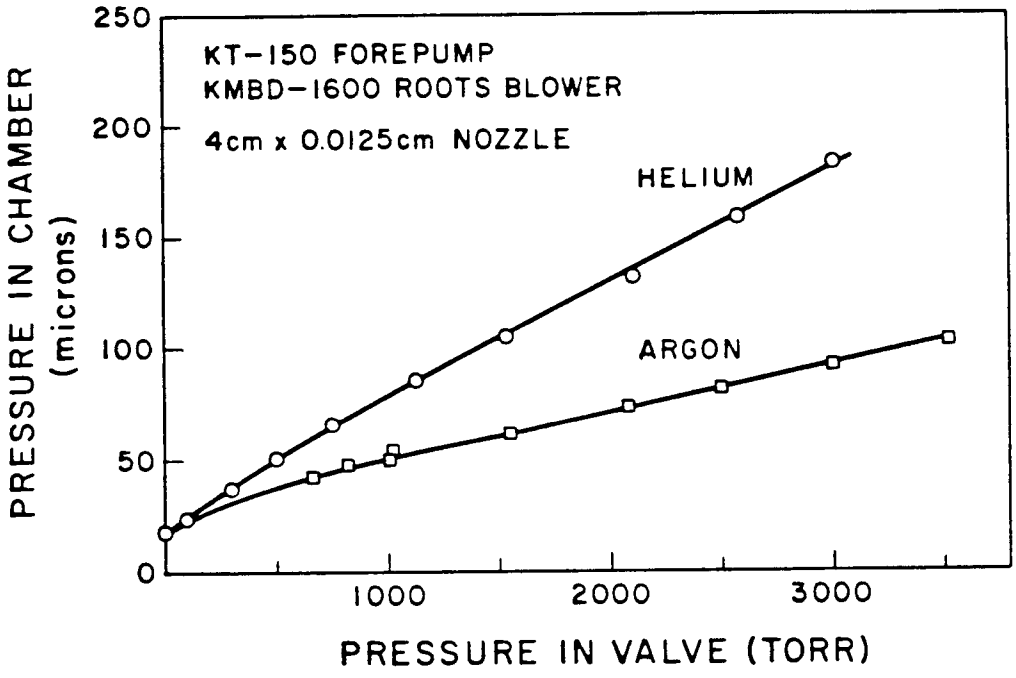

Figure 3.9 Background pressure in vacuum chamber during operation of slit valve.

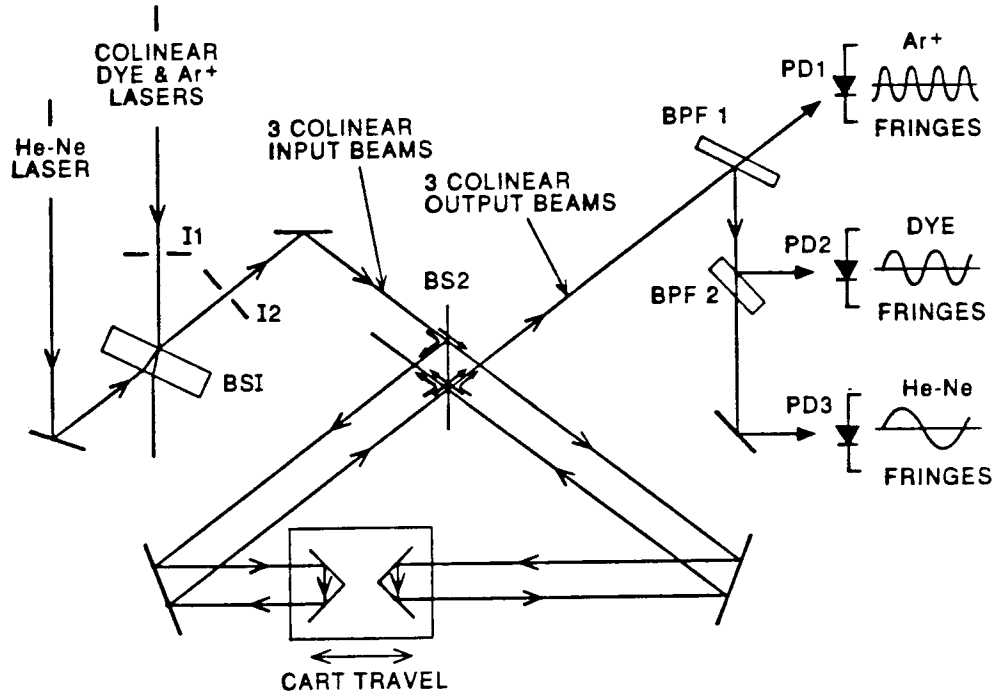

Figure 3.10 3-color laser λ-meter (Michelson interferometer).

combiner, and all three beams are simultaneously passed through the interferometer as shown. A beamsplitter separates the beams into two parts which travel through different arms of the interferometer, bounce off corner cubes, and are recombined on the same beamsplitter offset by ≈1.5 cm. The two corner cubes are mounted back-to-back on an air-bearing cart which travels ≈ 35 cm before the direction of travel is reversed by a solenoid-driven linear actuator. The lengths of the two arms of the interferometer are alternately lengthened and shortened by moving the cart back and forth along its track; one arm lengthens while the other shortens. The optical path difference between the two arms therefore changes by four times the cart travel.

The three recombined laser beams are subsequently separated by interference filters, and the fringes of each laser color are counted separately using photodiodes. As the interferometer pathlength difference is changed by ℓ, the number of interference fringes m_i counted for each laser is

$$m_i = \frac{2\Delta\ell}{\lambda_i} = \frac{2n_i\Delta\ell\ \omega_i}{c} \qquad (3.12)$$

where n_i is the refractive index of the laboratory air at frequency ω_i. The frequency of the Ar^+ or dye lasers ω_1 or ω_2

may then be obtained from the ratio

$$\frac{\omega_i}{\omega_3} = \frac{m_i n_3}{m_3 n_i} \tag{3.13}$$

The precision and accuracy of the frequency measurement is dependent on several factors, including 1) drift in the reference laser, 2) uncertainty in counting the fringes for each laser, 3) different optical paths for the unknown and reference beam, due to poor alignment collinearity and to different refractive indices for the reference and unknown color. We consider each factor separately, noting unresolved difficulties, then present a procedure which bypasses these difficulties.

Reference laser stability

The reference laser is a 633 nm He-Ne laser, constructed from a commercially produced laser tube and power supply in a home-built mount. The exact frequency of this (and any) laser depends on the length ℓ of the Fabry-Perot cavity formed by the end mirrors

$$\omega = \frac{nc}{2\ell} \tag{3.14}$$

where n is an integer ($\approx 0.38\times10^6$ for ℓ=12 cm) and c the speed of light. Temperature changes in the laboratory vary the length ℓ of the glass tube which supports the end mirrors, and thus

change the laser frequency. A conventional He-Ne laser may operate at any frequency within ≈ 0.01 cm^{-1} of the center of the gain curve, which sets a rather poor limit on the attainable precision and accuracy of a frequency measurement. However, by actively controlling the length of the cavity, the laser frequency may be easily stabilized to $\lesssim 0.0001$ cm^{-1}, as follows.

Changes in cavity length are detected by taking advantage of the fact that if the cavity length is short enough that two modes are lasing simultaneously, they will be orthogonally polarized. The two frequencies are thus readily separated by a polarization beamsplitter; comparing the powers of the two modes provides a measure of the offset from line center of the average of the two modes. This is shown schematically in Figure 3.11. When the power of both modes is equal, each is offset from the line center by the same amount. Warming the laser tube lengthens the cavity, decreasing the frequency of both modes but increasing the power of mode n+1 and decreasing the power of mode n, as shown in the figure. This imbalance is used to decrease the current passing through a heater, shortening the cavity and thus correcting the cause of the deviation. Similarly, cooling (shortening) of the tube is compensated by increasing the heater current. The laser frequency is thus controlled to $\pm$ 2 MHz for long periods, as

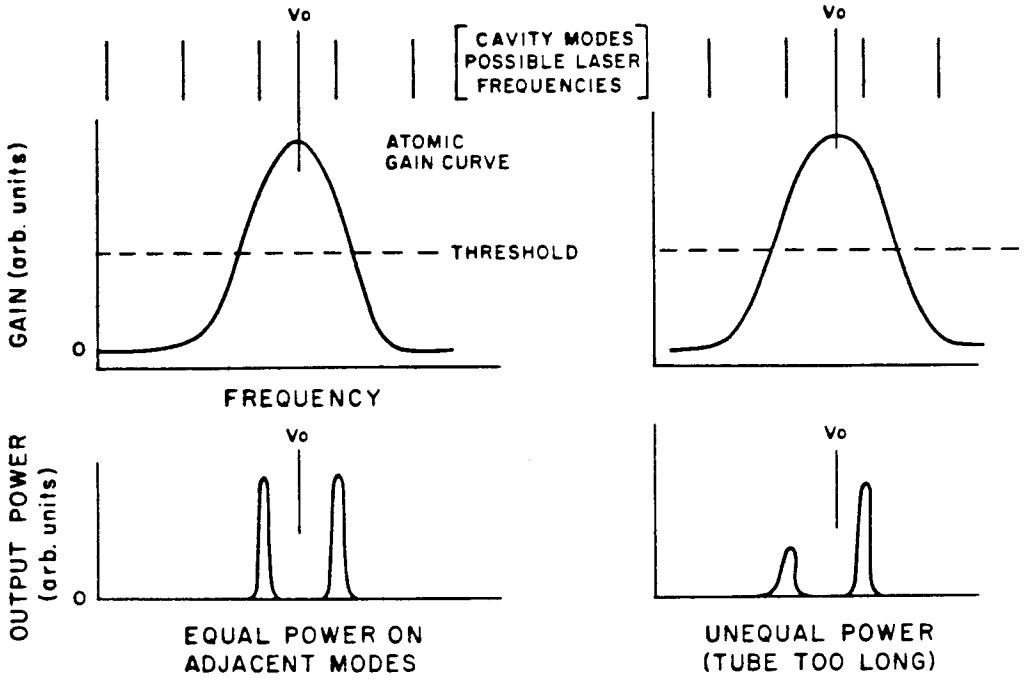

Figure 3.11 Polarization stabilized HeNe laser - cavity length determines power on adjacent modes.

determined by mixing the outputs of this "polarization-stabilized[8]" laser and the NIST (formerly NBS) standard, I_2-stabilized[9] HeNe on a fast photodiode, and recording the difference frequency as a function of time. The polarization stabilized laser was determined to operate 301.204 MHz to lower frequency than the standard which operates at 15798.00224 cm^{-1} or $4.736121925 \times 10^{14}$ Hz. The polarization stabilized laser frequency was therefore determined to be $4.736118913 \pm 10 \times 10^{14}$ Hz, or 15797.9922 cm^{-1}. Changes of laser tubes, alignment of the beamsplitter with respect to the laser, and other factors could shift this frequency by as much as 0.003 cm^{-1}, although such changes could in principle be monitored by periodic checking of the laser frequency against the primary standard. However, as we shall see below it is the moderate-term ($\approx$ minutes to hours) stability which is important, and this is unaffected by such changes.

Fringe counting uncertainty

The second source of interferometer frequency error is due to uncertainty in counting the number of reference and sample fringes. Two effects contribute to this uncertainty. First, it is easy to start and stop a counter which measures integral numbers of HeNe fringes, i.e. by triggering off the positive-going zero crossings, and similarly to count the number of Ar^+ or dye laser fringes during a preset number of HeNe

fringes. However, as shown schematically in Figure 3.12, in general the Ar^+ or dye laser fringes will neither start nor stop exactly in phase with the HeNe fringe. This leads to as much as a ±1 fringe error in counting sample fringes. For each determination the interferometer path length difference is changed by approximately 31 cm, producing $\approx 10^6$ HeNe fringes, so the error in fringe counting leads to 1 part in 10^6 or a ±0.016 cm^{-1} error in frequency measurement.

The measurement precision is increased by phase-locking a sixteen-fold higher frequency external oscillator to the sinusoidal interferometer signal for both the Ar^+ and dye lasers, and counting the zero crossings of the oscillator rather than the optical fringes. This increases the number of sample "fringes" to $1.5\text{-}2 \times 10^7$. The precision of each measurement is still ± one zero crossing, which now corresponds to an acceptable ±0.001 cm^{-1}. This uncertainty may be reduced by repeating the measurement and averaging the readings; for N measurements the uncertainty is reduced by $\sqrt{N}$ assuming that the error is random. Typically 36 measurements are averaged to achieve a reproducibility of 0.0002 cm^{-1}, comparable to the frequency uncertainty of the infrared laser. To decrease the response time of the readout during rapid adjustments of the laser frequency, 1/10 as many fringes are counted to a precision of 0.01 cm^{-1}.

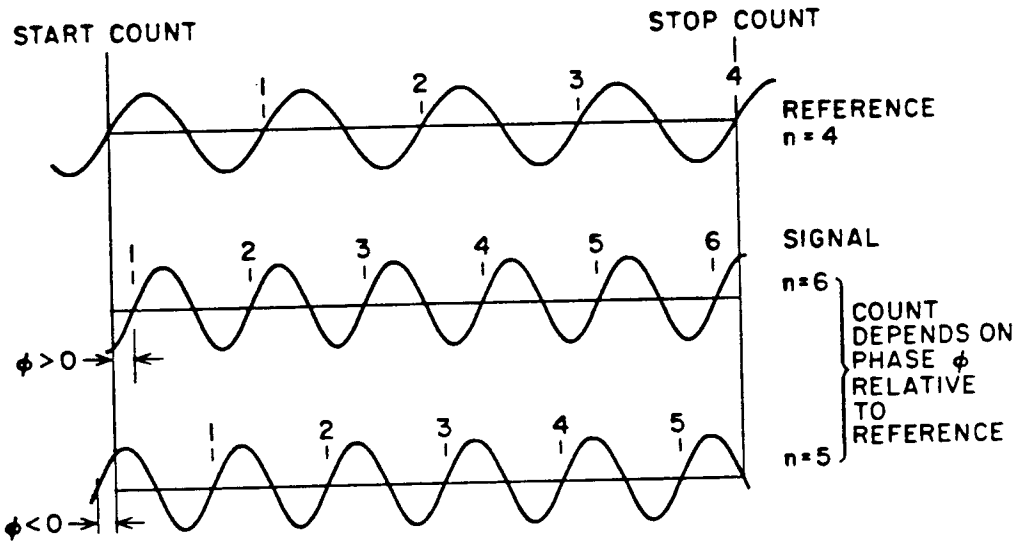

Figure 3.12 Source of interferometer fringe-counting error.

A second source of counting error is that in order for the number of sample fringes to be proportional to the actual frequency, we must count some integer number of fringes proportional to the reference laser frequency. For example, to display the frequency correct to 0.001 cm^{-1} would require counting 98737.4513 reference fringes, a non-integer number. We correct for this by counting (arbitrarily) 98738 reference fringes and m sample fringes, and correcting the displayed frequency (the integer m_i) using the formula

$$\omega_{corr} = (1 - \epsilon)\, m_i \tag{3.15}$$

where $\epsilon = 5.557 \times 10^{-6}$ for $\omega_{ref} = 15797.9922\ cm^{-1}$. Counting, e.g. 100 or 1000 times more sample and reference fringes would correspondingly reduce this correction factor, at the cost of unacceptably large measurement times (1-10 minutes).

Optical path length differences

The interferometric measurement of frequency assumes that the optical pathlength difference is the same for sample and reference beams. Two effects contribute to different optical path lengths for the sample and reference beams. In order of importance, these are 1) different refractive indices of air for the two colors, as implicitly shown in Eq. (3.12),

and 2) non-collinearity of sample and reference beams.

Table 3.2 shows the refractive index n_ω of air (Boulder pressure and typical laboratory temperatures) at selected wavelengths, and the correction to measured frequency required when using a HeNe laser as frequency reference. Note that the correction can change radically with temperature, pressure, and humidity, so that all three have to be measured to correct the frequency to ≈ 0.002 cm^{-1}. Table 3.3 shows a sample correction applied to a frequency measurement, at a frequency corresponding to the HF monomer R(0) transition. The infrared frequency is corrected by -0.0586 cm^{-1}, arriving at a value 0.0016 cm^{-1} too low. Sadly, this discrepancy might be attributable to errors in the refractive index correction (Ref. 10). Even more sadly, compiling a set of improved measurements would be a formidable undertaking.

To muddy the waters still further, the discrepancy might also be due to misalignment of the sample and reference beams. If the sample and reference beams are misaligned by an angle θ, the optical path difference for one of the beams will be $\cos(\theta)$ times that of the other. A misalignment of only 0.31×10^{-3} radians will introduce an error of 0.001 cm^{-1}! If the beams are aligned by passing through two apertures separated by the full length of the optical table ($\approx$ 3 meter), a misalignment of only 1.0 mm will introduce an error of 0.001 cm^{-1}. Due to

Table 3.2 Refractive index corrections[a] for HeNe reference.

λ, Å	$(n-1)\times10^4$	correction (cm^{-1})			
	(15°C, 620T) dry	(15°, 620T) dry	(15°, 620T) sat'd H_2O	(15°, 630T) dry	(25°, 620T dry
6328	2.252	0.0000	0.0000	0.0000	0.0000
6000	2.254	-0.0033	-0.0033	-0.0033	-0.0033
5800	2.256	-0.0069	-0.0069	-0.0069	-0.0066
5145	2.266	-0.0272	-0.0272	-0.0292	-0.0259
4880	2.271	-0.0389	-0.0389	-0.0408	-0.0371

a) Refractive indices from Reference 10.

Table 3.3 Sample frequency determination (in cm^{-1}).

	Ar^+ laser	dye laser	infrared
Measured	20486.8273	16485.7793	4001.0480
$\times (1-\epsilon)$[a]	20486.7135	16485.6877	4001.0258
refr. index[b]	-0.040	-0.002	4000.9878
literature[c]			4000.9894
error			-0.0016

a) See Eq. 3.15. b) Refractive index values from Ref. 10; pressure 634 Torr, temperature 22°C, relative humidity 11%.
c) Reference 11.

divergence of the laser beams, this 1.0 mm tolerance represents only ≈1/10 of the beam diameter. Alignment to this precision is possible but unlikely, so absolute frequency measurements to better than ≈ 0.002 cm^{-1} would seem to be unobtainable. In fact, lack of awareness of this extreme alignment sensitivity during the early days of my graduate career produced data sets each of which was self-consistent to ≲ 0.0005 cm^{-1}, but which differed between each other by up to 0.005 cm^{-1} (since a 3 meter alignment path length was not used). Clearly a solution to this difficulty was necessary.

A solution to the remaining problems

The above-mentioned difficulties in absolute wavelength measurements seem to suggest that measurement of infrared frequencies to better than ≈0.002 cm^{-1} is unlikely. However, the frequencies at which atoms or molecules absorb light do not change as a function of time, providing numerous references for relative frequency measurement. In other words, measurement of a known transition frequency provides at once a correction for all alignment, refractive index, and reference laser frequency uncertainties. By returning frequently to a frequency reference one may monitor all such error-inducing effects. In fact we have demonstrated repeatedly that changes of <0.0002 cm^{-1} over 6 hours are readily achieved if realignment of the laser and optical train is scrupulously avoided.

One can therefore correct for all sources of error except for the non-uniform refractive index of air for the dye laser frequency. The refractive index correction varies as the infrared laser frequency is tuned away from the molecular reference. However, as shown in Table 3.2 the refractive index correction for the dye laser is small, in fact it is negligible unless the frequency is changed by ≥ 40 cm^{-1}. In fact, as described below we are never further than 40 cm^{-1} from a frequency reference; over this range the maximum frequency uncertainty due to non-uniform refractive index is 0.0002 cm^{-1}. This possible source of error in the accuracy of an infrared frequency is typical of the precision of individual measurements, and thus is small enough to be ignored.

Two molecular references are used to provide absolute frequencies for the studies reported herein. For complexes of HF with the rare gases, the HF monomer frequencies of Guelachvili[11] are used; these are listed in Table 3.4. Guelachvili estimates that these frequencies are expected to be accurate to 0.0005 cm^{-1} and precise to 0.0003 cm^{-1}. An independent check of the relative frequencies of these transitions reveals that the precision is slightly better than this estimate. The frequency intervals between transitions sharing a common upper level (e.g. R(0) and P(2), which share

Table 3.4. Frequency references (in cm^{-1})[a].

	HF[b]	DF[c]	$H^{35}Cl$[d]	$H^{37}Cl$[d]
R(4)	4142.8460	3006.0912	-	-
R(3)	4109.9363	2987.4711	2963.2844	2961.0670
R(2)	4075.2936	2968.2050	2944.9124	2942.7207
R(1)	4038.9625	2948.3057	2925.8955	2923.7309
R(0)	4000.9894	2927.7864	2906.2457	2904.1097
ν_0[e]	3961.4229	2906.6609	2885.9754	2883.8694
P(1)	3920.3119	2884.9426	2865.0970	2863.0225
P(2)	3877.7075	2862.6457	2843.6235	2841.5816
P(3)	3833.6616	2839.7844	2821.5674	2819.5594
P(4)	3788.2277	2816.3739	2798.9418	2796.9690

a) Raw data, not corrected for refractive index correction.

b) Reference 11.

c) This work.

d) See the text.

e) Band origin, from a fit to polynomial in $[J(J+1)]^n$.

J'=1) are compared to the accurate ground state rotational term values of Jennings et al[12] in Table 3.5. The largest (observed-calculated) discrepancy is only 0.0002 cm^{-1}, approximately the reproducibility of the interferometric technique and therefore small enough to be ignored. The precision of these measurements is therefore adequate for a frequency standard. Whether or not the absolute frequencies are accurate will not be pursued here, however one should be aware that significantly different (up to 0.0015 cm^{-1}) transition frequencies are obtained using water vapor[13] as a calibrant.

Complexes of DF and HCl with the rare gases are measured relative to the methane ν_3 frequencies of Tarrago et al[16]. These frequencies are also expected to be accurate to 0.0005 cm^{-1} and precise to 0.0003 cm^{-1}. The accuracy is confirmed by noting that these authors reproduce (to -0.00011 cm^{-1}) the absolute frequency measurement of the methane $P(7F_1^{(2)})$ transition at 2947.91211 cm^{-1} by Evenson et.al.[17] The precision was confirmed in an exhaustive examination of the P(11) manifold. Frequency intervals between these transitions differed from the Tarrago et al values by a root-mean-square error of 0.00038(4) cm^{-1}, slightly outside the precision quoted above but acceptable if the average of several transitions is used.

Table 3.5 Monomer ground state combination differences (frequency intervals).

	observed	calculated	(obs.-calc.)
HF monomer			
R(0) - P(2)	123.2819	123.28210[a]	-0.0002
R(1) - P(3)	205.3009	205.30079	-0.0001
R(2) - P(4)	287.0659	287.06584	+0.0001
DF monomer			
R(0) - P(2)	65.1407	65.14094[b]	-0.0002
R(1) - P(3)	108.5213	108.52132	+0.0000
R(2) - P(4)	151.8311	151.83141	-0.0003
$H^{35}C\ell$ monomer			
R(0) - P(2)	62.6220	62.62218[c]	+0.0000
R(1) - P(3)	104.3280	104.32808	-0.0001
R(2) - P(4)	145.9720	145.97068	+0.0013
$H^{37}C\ell$ monomer			
R(0) - P(2)	62.5278	62.52814[c]	-0.0004
R(1) - P(3)	104.1719	104.17147	+0.0004
R(2) - P(4)	145.7519	145.75170	+0.0002

a) Reference 12

b) Reference 14, with centrifugal distortion value from present determination.

c) Reference 15.

Despite the advantages of such a frequency reference, it is inconvenient to keep on hand a supply of methane for a frequency reference. It is much more convenient to use HCl or DF as the frequency standard, since then one only has to tune the laser to a monomer transition rather than also introducing a new gas. However, the HCl transition frequencies of Guelachvili et al[18] are not consistent with the accurate methane frequencies of Tarrago et. al.[16] Since the methane P(11) manifold brackets the $H^{35}Cl$ monomer R(0) transition, we were able to determine to high precision a frequency of 2906.2457 ± 0.0002 cm^{-1}, which differs by -0.0019 cm^{-1} from the Guelachvili et al[18] value. However, ground state combination differences generated from the Guelachvili et al[18] data agree quite well with precise values determined from microwave and/or far-infrared spectroscopy, as shown in Table 3.5, confirming the precision of the measurements. In order to take advantage of the accurate frequency of my R(0) measurement, as well as the high precision of the Guelachvili et al measurements, we simply shift the latter by 0.0019 cm^{-1} to bring R(0) into agreement. The revised transition frequencies are listed in Table 3.4.

Clearly, with a frequency reference at most 40 cm^{-1} away the corrections for dye laser refractive index variations are negligible. However, if larger frequency intervals are measured it may be necessary to apply a correction. Figure 3.13 shows

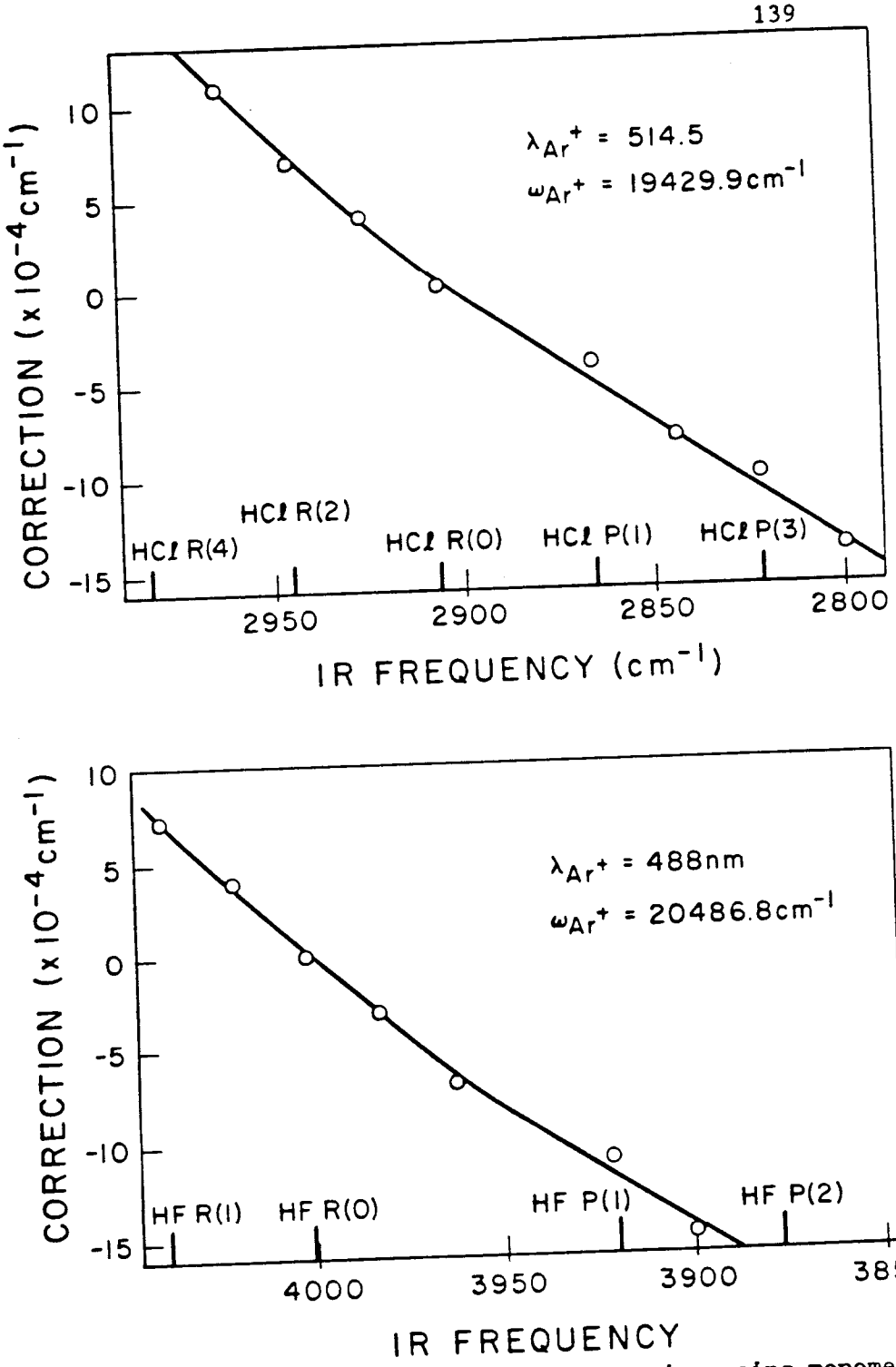

Figure 3.13 Corrections to infrared frequencies using monomer R(0) as a reference.

the errors introduced at different frequencies by using only the HF or HCl R(0) transition as a frequency reference. The largest correction on Figure 3.13 is ≈ 0.0014 cm^{-1}, or approximately seven times the measurement uncertainty.

Measurements in jets

The slit nozzle described above provides a medium with reduced Doppler linewidths and no measurable pressure broadening (<0.5 MHz). Typical infrared linewidths (full width at half maximum) are 0.0010 cm^{-1} (Ar diluent) to 0.0030 cm^{-1} (He diluent). The measurement reproducibility of 0.0002 cm^{-1} is thus at most 20% of the infrared linewidth. The laser frequency is controlled manually, with the operator attempting to maximize the time-dependent absorption displayed on an oscilloscope. Consequently, transition frequencies can be "skewed" by the operator if he preferentially samples either the low-frequency or high-frequency side of the line. Of course, as long as the operator treats all transitions equally, this shift will be the same for unknown and reference peaks, and will be subtracted.

Three circumstances have been noted which may affect this "equal treatment" method. First, if two or more persons are sharing the duty of measuring transition frequencies, it is necessary for each to determine his/her own calibration factor (i.e. the sum of alignment, reference laser offset, and refractive index correction). Second, even for a single operator the measured frequencies will initially not be

reproducible, changing by as much as 0.001 cm^{-1} over 5-8 repeated measurements. This is tentatively attributed to a "practice effect", whereby the necessary consistency is developed over a period of time. Conversely, after several hours of practice it is possible for a single operator to measure the same transition with a (maximum-minimum) spread for four measurements of $\lesssim$ 0.00005 cm^{-1}, a 20-fold improvement. Thus patience is required to develop maximum precision.

Third, measurement of optically black transitions (e.g. HF, DF, or HCl monomer R(0)) may tend to exacerbate the first two problems. This is because a relatively wide range of infrared frequencies ($\approx$ 0.001 - 0.0015 cm^{-1}) gives an equivalent signal (zero transmittance), making it difficult to locate the line center. It is convenient to supply to the valve a small amount of 1% monomer in diluent, then shut off the monomer and run pure diluent until the peak is too small to see (typically $\approx$ 10 minutes or 1-2 determinations). The problems arising from an optically black transition can also be minimized if a less intense transition (e.g. a van der Waals complex) is chosen for a secondary frequency reference. One transition per band, typically the P(1) transition for which $J' = 0$, is measured repeatedly with respect to the monomer. This peak then serves as a reference for measurement of adjacent peaks, both later in that day and on subsequent days. Needless to say, it is necessary to measure carefully the secondary frequency standard.

REFERENCES FOR CHAPTER III

1. A. S. Pine, J. Opt. Soc. Am. 64, 1683 (1974).

2. G. D. Boyd and A. Ashkin, Phys. Rev. 146, 187 (1966).

3. G. D. Boyd and D. A. Kleinman, J. Appl. Phys. 39, 3597 (1968).

4. J. U. White, J.Opt.Soc. Am. 32, 285, (1942).

5. A. W. Adamson, A Textbook of Physical Chemistry, (Academic, New York, 1973).

6. J. Finzi, (private communication).

7. J. L. Hall and S. A. Lee, Appl. Phys. Lett. 29, 367 (1976).

8. R. Balhorn, H. Kunzmann, and F. Lebowsky, Appl. Opt. 11, 742 (1972).

9. P. Lee and M. Skolnick, Appl. Phys. Lett. 10, 303 (1967).

10. R. C. Weast, Ed. CRC Handbook of Chemistry and Physics (CRC Press, Boca Raton, 1989).

11. G. Guelachvili, Opt. Commun. 19, 150 (1976).

12. D. A. Jennings, K. M. Evenson, L. R. Zink, C. Demuynck, J. L. Destombes, B. Lemoine, and J. W. C. Johns, J. Mol. Spectrosc. 122, 477 (1987).

13. C. Camy-Peyret, J. M. Flaud, G. Guelachvili, and C. Amiot, Mol. Physics, 26, 825 (1973).

14. P. Helminger, F. C. DeLucia, and W. Gordy, Phys. Rev. Lett. 25, 1397 (1970).

15. I. G. Nolt, J. V. Radostitz, G. DiLonardo, K. M. Evenson, D. A. Jennings, K. R. Leopold, M. D.Vanek, L. R. Zink, A. Hinz, and K. V. Chance, J. Mol. Spectrosc. 125, 274 (1987).

16. G. Tarrago, M. Dang-Nhu, G. Poussigue, G. Guelachvili, and C. Amiot, J. Molec. Spectrosc. 57, 246 (1975).

17. K. M. Evenson, J. S. Wells, F. R. Petersen, B. L. Danielson, G. W. Day, R. L. Barger, and J. L. Hall, Phys. Rev. Lett. 29, 1346 (1972).

18. G. Guelachvili, P. Niay, and P. Bernage, J. Molec. Spectrosc. 85, 271 (1981).